analytical chemistry

pubs.acs.org/ac Article

Superparamagnetic Nanostructures Coupled with an Entropy-Driven DNA Circuit for Elegant and Robust Photoelectrochemical Biosensing

Jing Li, Xuan Weng, Fan Mo, Min Han, and Hongbo Li*

Cite This: https://dx.doi.org/10.1021/acs.analchem.0c03580 Read Online

ACCESS | Metrics & More | Article Recommendations | Supporting Information

ABSTRACT: MicroRNA (miRNA) has become a key indicator of cancer diagnosis based on its abnormal expression levels. However, high-performance monitoring of miRNA is still a difficult task because of its low concentration, small size, and similarity of sequences. Herein, an elegant and robust photoelectrochemical (PEC) biosensor for miRNA-122 has been flexibly designed based on the split mode between entropy-driven DNA signal amplification and photocurrent expression. The entropy-driven DNA circuit uses a multichain composite structure instead of a DNA hairpin structure, leading to decrease the reversibility of each step of the signal amplification system. Also, the unique increasing entropy mechanism, rather than the free energy release from the new base pairs forming, improves the reaction efficiency and enhances more thermal stability and strong specific identification ability. Particularly, the biologically functionalized superparamagnetic Fe_3O_4@SiO_2 complex endows this split mode PEC biosensor with excellent specificity and enhanced efficiency of electrode fabrication. Additionally, this strategy of only the CdTe-signal DNA modified on the ITO electrode for photocurrent readout overcomes the shortcomings of tediously long layer-by-layer assembly process and multiple rinsing steps, leading to efficient improvement of the stability and reproducibility for the as-designed PEC biosensor. This elegant strategy opens a new path for miRNA measurements with superior performance.

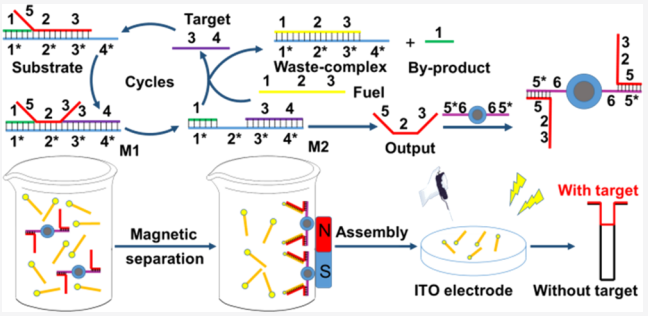

INTRODUCTION

MicroRNA (miRNA) can be a diagnostic indicator of cancer based on its abnormal expression level.[1,2] The early traditional miRNA detection methods mainly include northern blotting,[3] RT-PCR,[4,5] and microarrays.[6] Northern blotting has limited sensitivity and requires complex operation and radioisotope labeling, which seriously damages the environment. Although the RT-PCR and microarray methods have relatively high detection sensitivity, they are characterized by high production costs or complex operating procedures.[7] Recently, a variety of signal amplification techniques combined with various signal transducers such as fluorescence (FL),[8−10] electrochemiluminescence (ECL),[11,12] and surface-enhanced Raman scattering[13,14] have also been developed for highly sensitive measurement of miRNAs. However, these methods have at least one of the defects of enzyme inactivation, expensive equipment, complex fabrication, and limited specificity.[15−18] Therefore, it is desirable to develop a powerful sensor with comprehensive performance for low-abundance miRNAs.

For more than a decade, photoelectrochemical (PEC) assays[19−24] have become a fascinating technique due to low background noise and ultrasensitivity resulting from the separated optical excitation and signal readout. In addition to the sensitization strategies of photoelectric beacons such as dye-sensitized semiconductors,[25] heterojunction semiconductors,[26−28] cation-doped semiconductors,[29] Z-scheme mode,[30−32] and surface plasmon resonance-sensitized semiconductors,[33] biosignal amplification techniques such as enzyme-free catalytic hairpin assembly (CHA)[34] and hybridization chain reaction (HCR)[35,36] have also been integrated to PEC sensors. In the light of CHA and HCR strategies driven by free energy of DNA base pairs and request of a large amount of DNA hairpin structures, these cause the reaction system to be relatively sensitive to environmental conditions and prone to nonspecific binding.[37] Moreover, hairpin opening through chain hybridization is a reversible process that limits the application of these systems in complex biological systems. To overcome these drawbacks, entropy-driven signal amplification strategy based on dynamic DNA assembly is an alternative.[38] By using a multichain composite structure instead of a DNA hairpin structure, this entropy-driven strategy helps

Received: August 23, 2020
Accepted: October 21, 2020

to reduce the reversibility of each step in the signal amplification system. The unique increasing entropy mechanism, rather than the free energy release by forming new base pairs, improves the reaction efficiency and ensures that the base sequence remains unchanged during amplification.[39] Compared to those above amplification strategies, an entropy-driven DNA circuit also provides more thermal stability and strong specific identification ability for analysis. In addition, it can be designed flexibly based on specific targets. Recently, the energy transfer-based PEC sensor for miRNA-141 has been proposed by the combination of entropy-driven strategy and magnetic beads.[40] The application of magnetic beads helps to enhance the selectivity of the PEC biosensor by multiple extractions of the byproducts. However, this design is still complex in electrode fabrication, and also it cannot completely avoid the interference of target detection by coexisting species in complex biological samples. To address this issue, with the assistance of an external magnetic force, we reported that the target was identified and extracted by the superparamagnetic Fe_3O_4@SiO_2@TiO_2 particles functionalized by the probe, and the resulting composite was used for electrode modification and then the photocurrent measurement could be carried out in pure phosphate-buffered saline solution (PBS).[41] Herein, Fe_3O_4@SiO_2 is a nonconductor that prevents photogenerated electrons from being transferred to the ITO electrode and then reduces the photocurrent, resulting in limited sensitivity. Consequently, after magnetic enrichment and extraction in the liquid phase, further separating Fe_3O_4@SiO_2 from PEC signal expression is a potential way to construct a highly sensitive and specific PEC biosensor.

Herein, an elegant and robust PEC sensor for miRNA-122 as a model has been developed based on the separation of entropy-driven DNA circuit and signal expression (Scheme 1). Low-abundance miRNA-122 can efficiently trigger the increasing entropy system, and a large amount of output DNAs can be identified and facilely extracted by superparamagnetic Fe_3O_4@SiO_2 probe DNA. The resulting Fe_3O_4@SiO_2 probe DNA-output DNA composite was further utilized to capture CdTe-signal DNA in the flask based on the Watson−Crick base-pairing rule. Only in the presence of miRNA-122, the liberated output DNA could act as a bridge to promote the formation of Fe_3O_4@SiO_2 probe DNA-output DNA-signal DNA-CdTe composite, which can be extracted by an external magnetic force and result in the proportional reduction of CdTe-signal DNA in the flask and then the decreased photocurrent. The magnetic separation of biologically functionalized Fe_3O_4@SiO_2 particles helps forming an elegant and split mode PEC biosensor with only a one-step electrode assembly procedure, which endues the advantages of the as-designed PEC biosensor with excellent selectivity and sensitivity, high efficiency of electrode preparation, flexibility, and simplicity. Moreover, in addition to the controlled monodisperse functional nanomaterials used in the as-designed PEC sensor, this elegant strategy avoids the layer-by-layer assembly and multiple electrode rinsing steps, endowing the PEC biosensor with excellent stability and reproducibility. Additionally, the unique entropy-driven signal amplification strategy and the deliberate separation of the insulator Fe_3O_4@SiO_2 from the photocurrent readout make the miRNA-122 PEC biosensor ultrasensitive. This exclusive strategy can be flexibly designed for a variety of miRNAs.

Scheme 1. (A) Schemes of Entropy-Driven DNA Signal Amplification System and (B) PEC Signal Readout for miRNA-122

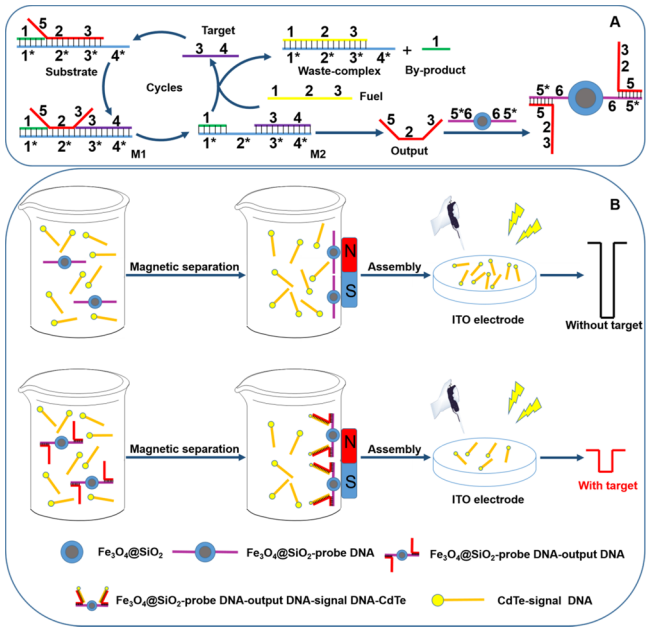

EXPERIMENTAL SECTION

Preparation of Fe_3O_4@SiO_2 Probe DNA. The mixture containing 500 μL of Fe_3O_4@SiO_2, 30 mL of ethanol, and 50 μL of APTES was heated at 80 °C for 3 h under nitrogen condition, and the resulting product was washed twice with ethanol and water, respectively. Then, the generated Fe_3O_4@SiO_2−NH_2 particles were redispersed in 500 μL water. Meanwhile, 200 μL of 0.1 mol L^{-1} EDC and NHS was added in 500 μL of 1.5 μmol L^{-1} probe DNA solution, and reacted for 3 h at 25 °C, and then the above Fe_3O_4@SiO_2 suspension was scattered into the mixture and reacted at 25 °C for 4 h. Afterward, the resulting product was washed three times with water and then redispersed in 500 μL buffer solution for the following use.

Preparation of CdTe-Signal DNA. The mixture containing 200 μL of 0.1 mol L^{-1} EDC and NHS was added in 500 μL of 3.6 μmol L^{-1} CdTe QD solution and reacted at 25 °C for 3 h. Then, 500 μL of 1.5 μmol L^{-1} signal DNA was added and stirred at 25 °C for 4 h. Afterward, it was stored at 4 °C.

Construction of the PEC Biosensor. First, the mixture containing 50 μL of 1.2 μmol L^{-1} output strands, byproduct strands, and scaffold strands was heated at 95 °C for 5 min and then cooled to 4 °C for 1 min for the following use. Then, 50 μL of the resulting substrate complex (0.4 μmol L^{-1}) was added in the same volume of a certain concentration of target and reacted at 25 °C for 2 h. As a result, a four-stranded metastable complex M1 was formed by a toehold-mediated strand displacement reaction. Subsequently, M1 was converted to M2 with the release of output DNA. Next, 50 μL of 0.4 μmol L^{-1} fuel DNA was added in the system and reacted at 25 °C for 2 h. The introduction of fuel DNA enables the generation of waste complex, target, and byproduct. Meanwhile, the regenerated target triggers the next round of reaction. After the entropy-driven signal amplification process, 50 μL of the prepared Fe_3O_4@SiO_2 probe DNA complex was scattered into the above system and reacted at 25 °C for 2 h.

https://dx.doi.org/10.1021/acs.analchem.0c03580
Anal. Chem. XXXX, XXX, XXX−XXX

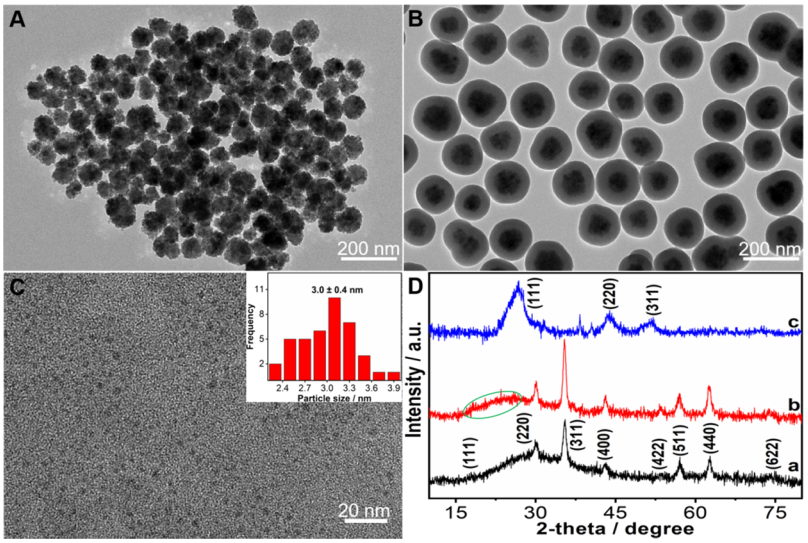

Figure 1. (A) HRTEM images of Fe_3O_4, (B) Fe_3O_4@SiO_2, and (C) CdTe particles. (D) X-ray diffraction (XRD) spectra of panels (a–c).

Then, the resulting Fe_3O_4@SiO_2 probe DNA-output DNA complex was extracted by an external magnetic force. After washing twice, it was scattered into 50 μL of the prepared CdTe-signal DNA solution and reacted at 25 °C for 2 h. Following, the resulting Fe_3O_4@SiO_2 probe DNA-output DNA-CdTe-signal DNA complex was extracted with the assistance of an external force, and 20 μL of the supernatant (the reduced concentration of CdTe-signal DNA solution) was cast on a clean ITO electrode. After drying at 25 °C, the prepared electrode was utilized for the photoelectric signal measurement in 0.1 mol L^{-1} PBS (pH 7.0). For the controlled experiment, the operating steps are the same with above except for the absence of target miRNA-122.

RESULTS AND DISCUSSION

Characterization of the Synthesized Nanomaterials. The morphologies and structures of the functional nanomaterials were imaged by HRTEM (Figure 1). As shown in Figure 1A, the mean size of the prepared Fe_3O_4 colloidal nanocrystalline clusters is about 90 nm in diameter. After the coating of SiO_2, the size increases to ~165 nm in diameter (Figure 1B and Figure S1). Also, Figure 1C shows that the average size of CdTe QDs is approximately 3.0 nm. In order to further determine the structure of the above materials, XRD patterns have been performed (Figure 1D). As is shown, curve a shows that the diffraction peaks at 18.3 (111), 30.1 (220), 35.4 (311), 43.1 (400), 53.4 (422), 56.9 (511), 62.5 (440), and 74.9° (622), which are consistent with those of the magnetite Fe_3O_4 phase (JCPDS 19-0629). Compared to curve a, there is a new wide peak that appears at 16–29° (curve b), suggesting the coating of colloidal SiO_2 (JCPDS 29-0085).[41] The structure of the resulting Fe_3O_4@SiO_2 was also confirmed by XPS characterization (Figure S3). Additionally, the superparamagnetic characteristics of Fe_3O_4 and Fe_3O_4@SiO_2 particles were proved by magnetic hysteresis loops (Figure S4). Curve c in Figure 1D shows that the diffraction peaks at 26.70, 43.80, and 51.60° can be assigned to (111), (220), and (311) planes of CdTe QDs.[42] Also, the UV–vis absorbance and fluorescence emission spectra of CdTe QDs were recorded (Figure S2). These indicate that the CdTe QDs have been successfully prepared.

Construction and Evaluation of Entropy-Driven Signal Amplification System. The low-abundance target (T) can efficiently trigger the entropy-driven signal amplification system (Scheme 1). Specifically, the scaffold strand comprises a single-stranded toehold, termed as 4*, which can be combined with T and generate a four-stranded metastable complex M1, which is achieved by replacing domain 3 on O. Consequently, a new three-strand complex M2 was formed since T is fully bound with the scaffold strand. When F was introduced to completely bind with the scaffold strand in M2, B was regenerated simultaneously. Meanwhile, T was also released to trigger a new round of entropy-driven signal amplification process. The whole system is driven by increasing entropy because there is no change in the number of base pairs for each individual catalytic cycle.

Native polyacrylamide gel electrophoresis (PAGE) was utilized to examine the conversion process of target triggering the three-chain-structured substrate (Scheme 1). As shown in Figure 2, the purified scaffold strand, B, and O show sharp and neat bands in lane 1, lane 2, and lane 3, respectively. After the reaction of the same concentration of the scaffold strand, B, and O, a toehold-mediated strand migration appeared (lane 4), indicating the formation of a three-chain structured substrate. Compared to the band in lane 4, two additional bands occurred in lane 5 in the presence of a low concentration of T (0.01×), indicating that part of the three-chain-structured substrate was converted to waste complex M2 and O. Also, compared to the bands in lane 5, by the trigger of the same concentration of F, the newly generated two bands can be assigned to the residual F and B. The bands of the M3 and S cannot be separated due to their similar amount of DNA bases (lane 6). Also, the band of the released T cannot be observed due to the trigger of next entropy-driven signal amplification process.

Thermodynamic Calculation of Increasing Entropy System. As shown in Figure 3, the reaction equation gives expression to the whole increasing entropy process with the parameters marked. The reaction process controlled by thermodynamic theory is verified by the following formulas. In the diluted solution, for this reaction, the change in Gibbs free energy is

https://dx.doi.org/10.1021/acs.analchem.0c03580
Anal. Chem. XXXX, XXX, XXX–XXX

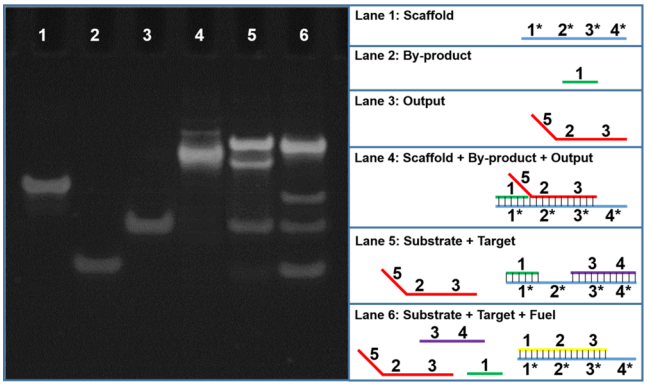

Figure 2. Native PAGE characterization of the DNA amplifier system. Lane 1: scaffold: 5 μmol L^{-1} × 5 μL; lane 2: byproduct: 5 μmol L^{-1} × 5 μL; lane 3: output: 5 μmol L^{-1} × 5 μL; lane 4: scaffold: 5 μmol L^{-1} × 5 μL + byproduct: 50 μmol L^{-1} × 0.5 μL + output: 50 μmol L^{-1} × 0.5 μL; lane 5: scaffold: 5 μmol L^{-1} × 5 μL + byproduct: 50 μmol L^{-1} × 0.5 μL + output: 50 μmol L^{-1} × 0.5 μL + target: 0.5 μmol L^{-1} × 0.5 μL (0.01 ×); lane 6: scaffold: 5 μmol L^{-1} × 5 μL + byproduct: 50 μmol L^{-1} × 0.5 μL + output: 50 μmol L^{-1} × 0.5 μL + target: 0.5 μmol L^{-1} × 0.5 μL (0.01 ×) + fuel: 50 μmol L^{-1} × 0.5 μL. Reaction time = 2 h.

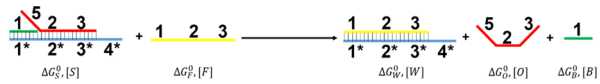

Figure 3. Reaction equation of the entropy-driven DNA signal amplification system with thermodynamic parameters marked.

$$\Delta G = \Delta H - T\Delta S \quad (1)$$

Herein, ΔH and ΔS represent the change of system enthalpy and entropy, respectively. T refers to the thermodynamic temperature. The sum of the base pairs remains the same throughout the reaction system, and as a result $\Delta H \approx 0$. Consequently, the reaction is driven by an increase in the entropy ($T\Delta S$) of the released molecule.

Then, in this increasing entropy system, the final concentration of each species can be calculated. The following formula gives the change of Gibbs free energy.

$$\Delta G = \Delta G_B^0 + \Delta G_O^0 + \Delta G_W^0 - \Delta G_S^0 - \Delta G_F^0 + RT \ln Q \quad (2)$$

ΔG_X^0 is the standard free energy of the X species under standard conditions, and its unit is expressed in kcal/mol. Also, the value can be obtained by the free software Nupack.[43]

$$\Delta G_B^0 + \Delta G_O^0 + \Delta G_W^0 - \Delta G_S^0 - \Delta G_F^0 = -13.49 \text{ kcal/mol} \quad (3)$$

When the reaction is balanced, this means that the value of ΔG is 0, and the Q value of 3.13 can be calculated according to eqs 2 and 3.

Herein, Q represents the reaction quotient, and it can be depicted by $Q = \{([B]/c^0)([O]/c^0)([W]/c^0)\}/\{([S]/c^0)([F]/c^0)\}$, where c^0= 1 mol L^{-1}. The initial concentrations of S and F are 100 nmol L^{-1}, and the final concentration of O is X, and then the following equation can be listed.

$$\frac{(10^{-9}X)^3}{[10^{-9}(100 - X)]^2} = 3.13$$

Consequently, X is calculated to be 99.98−99.99 nmol L^{-1} by bisection technique. This means that the system conversion rate is over 99.98%, regardless of reaction time.

PEC Working Mechanism. Based on the construction and evaluation of entropy-driven signal amplification system by PAGE and thermodynamic calculation, the PEC working mechanism can be proposed (Scheme 1). Specifically, after 5 pmol L^{-1} target miRNA-122 efficiently triggers the entropy-driven signal amplification process, a great deal of released output DNA was hybridized onto the Fe_3O_4@SiO_2 probe DNA composite (Figure S5A). With the assistance of an external magnetic force, the resulting Fe_3O_4@SiO_2 probe DNA-output DNA complex was extracted and washed several times with buffer solution. Then, it was scattered into the CdTe-signal DNA (Figure S5B) solution for hybridization. As a result, the concentration of CdTe-signal DNA solution was decreased since the resulting Fe_3O_4@SiO_2 probe DNA-output DNA-CdTe-signal DNA complex was extracted by an external magnetic field (Figure 4B). This resulted in the decrease of CdTe-signal DNA complex modified on the ITO electrodes and then the decreased photocurrent response (101.3 nA). For the controlled experiment (Figure 4A), in the absence of target miRNA-122, the system does not produce output DNA acting as a bridge, which prevents the Fe_3O_4@SiO_2 probe DNA from capturing CdTe-signal DNA. In other words, low-abundance miRNA-122 can efficiently trigger the increasing entropy system, and a large amount of the liberated output DNAs can be identified and extracted by superparamagnetic Fe_3O_4@SiO_2 probe DNA with the assistance of an external magnetic field. The resulting composite Fe_3O_4@SiO_2 probe DNA-output DNA scattered in the CdTe-signal DNA solution can further form the Fe_3O_4@SiO_2 probe DNA-output DNA-signal DNA-CdTe composite based on the Watson−Crick base-pairing rule. After further magnetic extraction, the concentration of the

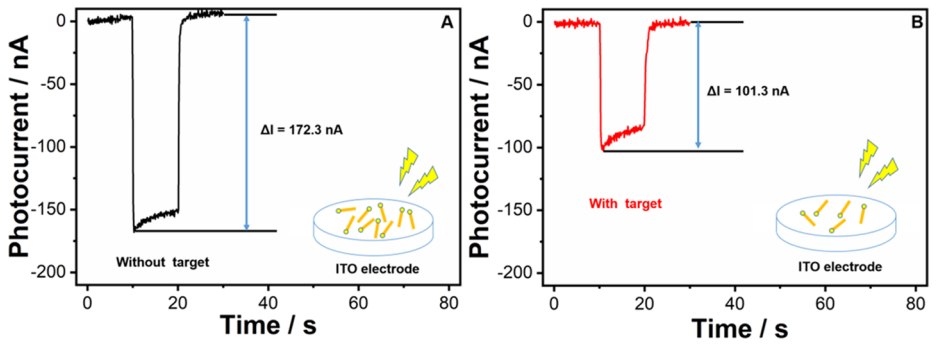

Figure 4. Photocurrent responses of the as-designed PEC biosensor (A) without and (B) with 5 pmol L^{-1} miRNA-122.

https://dx.doi.org/10.1021/acs.analchem.0c03580
Anal. Chem. XXXX, XXX, XXX−XXX

CdTe-signal DNA in the flask was decreased, and a certain amount of them modified on ITO electrodes would result in photocurrent decrease in a proportional manner. Therefore, it can be concluded that low-abundance target miRNA-122 can be monitored based on this unique working mechanism.

Analytical Performance. The as-designed PEC biosensor was utilized for the measurement of target miRNA-122 based on the separation of entropy-driven signal amplification and photocurrent expression. As shown in Figure 5A, the photocurrent decreases gradually as the concentration of target increases. The calibration curve is obtained by linear fitting, resulting in a dynamic range between 100 amol L^{-1} and 5 pmol L^{-1} (Figure 5B) with a detection limit of 94.2 amol L^{-1} at 3 S/N, which is almost advantageous over all those electrochemical,[15,44−46] ECL,[47] fluorescence,[48,49] high-performance liquid chromatography−fluorescence (HPLC-FL),[50] and PEC[51−53] approaches (Table 1). The ultrasensitivity mainly benefits from the entropy-driven signal amplification system and the inherent characteristics of PEC analytical technique. Moreover, compared to the conventional PEC sensor designs,[20−24] the as-designed PEC biosensor possesses good performance in efficiency, flexibility, and simplicity, which benefits from the split mode design that avoids the various modified materials layer-by-layer assembly on the surface of electrodes.

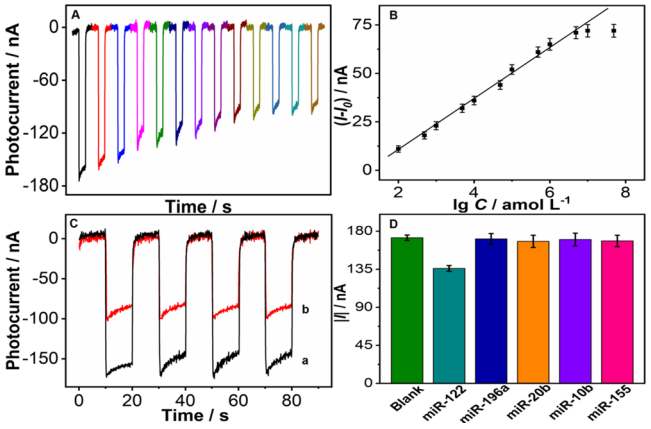

Figure 5. (A) Photocurrent responses of the as-designed PEC biosensor for various concentrations of miRNA-122: 0, 1×10^2, 5×10^2, $1 \times 10,^3$ 5×10^3, 1×10^4, 5×10^4, 1×10^5, 5×10^5, 1×10^6, 5×10^6, 1×10^7, and 5×10^7 amol L^{-1}. (B) Corresponding calibration curve. (C) Photocurrent responses of the as-designed PEC sensor (A) in the absence of and (B) presence of 5 pmol L^{-1} miRNA-122 with continuous "off−on−off" light irradiation for four cycles. (D) Photocurrent responses of the as-designed biosensor in the presence of 1 pmol L^{-1} miRNA-122, 500 pmol L^{-1} miRNA-155, miRNA-196a, miRNA-20b, and miRNA-10b.

The stability of this PEC biosensor was evaluated by four consecutive "off−on−off" light radiations (Figure 5C). As is shown, the photocurrents almost remain the same in the absence and presence of 5 pmol L^{-1} miRNA-122, indicating the stability of the as-designed PEC biosensor. Also, when the PEC biosensor was not in use, it was stored at 4 °C. When measured weekly, the photocurrent was almost unchanged in the first three weeks, and it still can maintain 95.1% of the initial value after five weeks, suggesting that the PEC biosensor holds excellent long-term stability (Figure S6), which benefits from the split-type design and then only the CdTe-signal DNA modified on the ITO electrode for signal readout. The reproducibility of the PEC biosensor was also assessed by seven freshly prepared PEC biosensors. The relative standard deviation (RSD) of 5.3% can be worked out from the calibration curves in Figure 5B, suggesting that the PEC biosensor is repeatable. These benefit from the controlled monodisperse functional nanomaterials and one-step electrode assembly, which overcomes the shortcoming of multiple rinsing steps for the modified electrodes.[22,25,35,36]

Selectivity is a significant parameter, and it has been evaluated by adding the individual coexisting species with 500 times the concentration of miRNA-122 (1 pmol L^{-1}) (Figure 5D). As is shown, the changed photocurrent was no more than 5.2%, indicating that the as-designed PEC biosensor has excellent specificity. It benefits from magnetic separation of biologically functionalized superparamagnetic Fe_3O_4@SiO_2, the Watson−Crick base-pairing rule, and the rationally designed split mode between entropy-driven signal amplification and photocurrent readout. Also, the entropy-driven signal amplification system contributes to remain the base number unchanged, which is in favor of improving the specificity of the PEC biosensor.[39,40]

To assess the practicality of the PEC biosensor applied in human serum samples, the standard addition method was selected to carry out the recovery experiment (Figure S7). The implementation is consistent with the construction of PEC biosensors, except that human serum replaces the standard solution of the same volume. The results showed that the recovery ranges from 93.7 to 102.1%, and the RSD is between 4.37 and 4.79% (Table 2), indicating that the accuracy of the

Table 1. Comparison of Different Measurement Methods of miRNAs

method	linear range	limit of detection	references
electrochemical	$1 \times 10^{-16} \sim 1 \times 10^{-7}$ mol L^{-1}	5.3×10^{-17} mol L^{-1}	44
electrochemical	$1 \times 10^{-16} \sim 1 \times 10^{-9}$ mol L^{-1}	1×10^{-16} mol L^{-1}	45
electrochemical	$1 \times 10^{-16} \sim 1 \times 10^{-10}$ mol L^{-1}	1×10^{-16} mol L^{-1}	46
ECL	$1 \times 10^{-14} \sim 1 \times 10^{-8}$ mol L^{-1}	1.5×10^{-15} mol L^{-1}	47
FL	$5 \times 10^{-10} \sim 5 \times 10^{-8}$ mol L^{-1}	7.2×10^{-11} mol L^{-1}	48
FL	$1 \times 10^{-13} \sim 1 \times 10^{-9}$ mol L^{-1}	4.4×10^{-14} mol L^{-1}	49
HPLC-FL	$1 \times 10^{-15} \sim 1 \times 10^{-10}$ mol L^{-1}	3.9×10^{-16} mol L^{-1}	50
PEC	$1 \times 10^{-15} \sim 1 \times 10^{-10}$ mol L^{-1}	3.1×10^{-16} mol L^{-1}	51
	$1 \times 10^{-15} \sim 1 \times 10^{-11}$ mol L^{-1}	2.9×10^{-16} mol L^{-1}	
PEC	$1 \times 10^{-15} \sim 1 \times 10^{-10}$ mol L^{-1}	4.7×10^{-16} mol L^{-1}	52
PEC	$5 \times 10^{-16} \sim 5 \times 10^{-12}$ mol L^{-1}	1.3×10^{-16} mol L^{-1}	53
PEC	$1 \times 10^{-16} \sim 5 \times 10^{-12}$ mol L^{-1}	9.42×10^{-17} mol L^{-1}	this work

https://dx.doi.org/10.1021/acs.analchem.0c03580
Anal. Chem. XXXX, XXX, XXX−XXX

as-designed PEC biosensor is competent for the practical setting.

Table 2. Proposed PEC Biosensor Was Used for the Detection of miRNA-122 in Serum Samples (n = 4)[a]

serum sample	added (fmol L^{-1})	found (fmol L^{-1})	recovery (%)	RSD (%)
1	0			
2	10	9.37	93.7	4.37
3	100	102.1	102.1	4.79
4	1000	973.6	97.4	4.54

[a] n is the repetitive measurement number.

CONCLUSIONS

In summary, a flexible and rational split mode of entropy-driven amplifiers and photocurrent readout has been selected for the development of miRNA-122 PEC biosensing. The entropy-driven amplification system has been confirmed by PAGE characterization and thermodynamic calculation. This entropy-driven strategy efficiently reduces the reversibility of the signal amplification process due to the application of a multichain composite structure. Also, the exclusive increasing entropy endows the PEC analysis with advantages of high reaction efficiency, more thermal stability, and strong specificity. In particular, this unique split mode successfully overcomes the drawback of tediously long layer-by-layer assembly of electrode materials. Herein, the functionalized superparamagnetic Fe_3O_4@SiO_2 complex plays a key role for the separation of entropy-driven DNA amplifiers and signal readout, leading to the improved selectivity of the PEC biosensor and the efficiency of the electrode fabrication. Additionally, this unparalleled strategy achieves the signal readout by only the photoelectric beacon assembled on the ITO electrode. This contributes to the enhanced stability, reproducibility, as well as the sensitivity for the novel PEC biosensor. This well-designed split mode PEC biosensor will provide a new perspective for measuring various miRNAs.

ASSOCIATED CONTENT

Supporting Information

The Supporting Information is available free of charge at https://pubs.acs.org/doi/10.1021/acs.analchem.0c03580.

Reagents, apparatus, synthesis of Fe_3O_4 nanoclusters, Fe_3O_4@SiO_2 particles, CdTe QDs, and partial characterizations (PDF)

AUTHOR INFORMATION

Corresponding Author

Hongbo Li − *School of Chemistry and Chemical Engineering, Yancheng Institute of Technology, Yancheng 224051, PR China;* orcid.org/0000-0001-8662-0427; Phone: +86-515-88298735; Email: hbli@ycit.edu.cn

Authors

Jing Li − *School of Chemistry and Chemical Engineering, Yancheng Institute of Technology, Yancheng 224051, PR China*

Xuan Weng − *School of Chemistry and Chemical Engineering, Yancheng Institute of Technology, Yancheng 224051, PR China*

Fan Mo − *School of Chemistry and Chemical Engineering, Yancheng Institute of Technology, Yancheng 224051, PR China*

Min Han − *School of Chemistry and Chemical Engineering, Yancheng Institute of Technology, Yancheng 224051, PR China*

Complete contact information is available at: https://pubs.acs.org/10.1021/acs.analchem.0c03580

Notes

The authors declare no competing financial interest.

ACKNOWLEDGMENTS

We acknowledge the financial support from the Natural Science Foundation of China (21505117 and 21775135), the Natural Science Foundation of Jiangsu Province (BK20161309), and this work was also sponsored by Qinglan Project of Jiangsu Province.

REFERENCES

(1) Lagos-Quintana, M.; Rauhut, R.; Lendeckel, W.; Tuschl, T. *Science* **2001**, *294*, 853−858.

(2) Kore, A.; Hodeib, M.; Hu, Z. *Nucleosides, Nucleotides Nucleic Acids* **2008**, *27*, 1−17.

(3) Várallyay, É.; Burgyán, J.; Havelda, Z. *Nat. Protoc.* **2008**, *3*, 190−196.

(4) Feng, W.; Newbigging, A. M.; Le, C.; Pang, B.; Peng, H.; Cao, Y.; Wu, J.; Abbas, G.; Song, J.; Wang, D.-B.; Cui, M.; Tao, J.; Tyrrell, D. L.; Zhang, X.-E.; Zhang, H.; Le, X. C. *Anal. Chem.* **2020**, *92*, 10196−10209.

(5) Kim, S. C.; Clark, I. C.; Shahi, P.; Abate, A. R. *Anal. Chem.* **2018**, *90*, 1273−1279.

(6) Yin, J. Q.; Zhao, R. C.; Morris, K. V. *Trends Biotechnol.* **2008**, *26*, 70−76.

(7) Peng, H.; Newbigging, A. M.; Reid, M. S.; Uppal, J. S.; Xu, J.; Zhang, H.; Le, X. C. *Anal. Chem.* **2020**, *92*, 292−308.

(8) Ma, F.; Zhang, Q.; Zhang, C.-Y. *Nano Lett.* **2019**, *19*, 6370−6376.

(9) Li, N.; Li, R.; Li, Z.; Yang, Y.; Wang, G.; Gu, Z. *Sens. Actuators, B* **2019**, *283*, 666−676.

(10) Cheng, Y. Y.; Xie, Y. F.; Li, C. M.; Li, Y. F.; Huang, C. Z. *Anal. Chem.* **2019**, *91*, 11023−11029.

(11) Zhang, Y.; Chai, Y.; Wang, H.; Yuan, R. *Anal. Chem.* **2019**, *91*, 14368−14374.

(12) Lu, L.; Wang, J.; Miao, W.; Wang, X.; Guo, G. *Anal. Chem.* **2019**, *91*, 1452−1459.

(13) Wang, Z.; Ye, S.; Zhang, N.; Liu, X.; Wang, M. *Anal. Chem.* **2019**, *91*, 5043−5050.

(14) Wen, S.; Su, Y.; Dai, C.; Jia, J.; Fan, G.-C.; Jiang, L.-P.; Song, R.-B.; Zhu, J.-J. *Anal. Chem.* **2019**, *91*, 12298−12306.

(15) Islam, M. N.; Masud, M. K.; Haque, M. H.; Hossain, M. S. A.; Yamauchi, Y.; Nguyen, N.-T.; Shiddiky, M. J. A. *Small Methods* **2017**, *1*, 1−20.

(16) Masud, M. K.; Umer, M.; Hossain, M. S. A.; Yamauchi, Y.; Nguyen, N.-T.; Shiddiky, M. J. A. *Trends Biochem. Sci.* **2019**, *44*, 433−452.

(17) Masud, M. K.; Na, J.; Younus, M.; Hossain, M. S. A.; Bando, Y.; Shiddiky, M. J. A.; Yamauchi, Y. *Chem. Soc. Rev.* **2019**, *48*, 5717−5751.

(18) McDonald, J. S.; Milosevic, D.; Reddi, H. V.; Grebe, S. K.; Algeciras-Schimnich, A. *Clin. Chem.* **2011**, *57*, 833−840.

(19) Li, J.; Xu, L.; Shen, Y.; Guo, L.; Yin, H.; Fang, X.; Yang, Z.; Xu, Q.; Li, H. *Anal. Chem.* **2020**, *92*, 8607−8613.

(20) Chu, Y.; Wu, R.; Fan, G. C.; Deng, A. P.; Zhu, J. J. *ACS Sustainable Chem. Eng.* **2018**, *6*, 11633−11641.

(21) Guo, L.; Yin, H.; Xu, M.; Zheng, Z.; Fang, X.; Chong, R.; Zhou, Y.; Xu, L.; Xu, Q.; Li, J.; Li, H. *ACS Sens.* **2019**, *4*, 2724−2729.

(22) Shu, J.; Tang, D. *Anal. Chem.* **2020**, *92*, 363−377.

(23) Yang, X.; Gao, Y.; Ji, Z.; Zhu, L. B.; Yang, C.; Zhao, Y.; Shu, Y.; Jin, D.; Xu, Q.; Zhao, W. W. *Anal. Chem.* **2019**, *91*, 9356−9360.

(24) Ma, W.; Ma, H.; Peng, Y. Y.; Tian, H.; Long, Y. T. *Nat. Protoc.* **2019**, *14*, 2672−2690.
(25) Li, M.; Xiong, C.; Zheng, Y.; Liang, W.; Yuan, R.; Chai, Y. *Anal. Chem.* **2018**, *90*, 8211−8216.
(26) Gao, X.; Cai, Q.; Li, H.; Jie, G. *Anal. Chem.* **2020**, *92*, 6734−6740.
(27) Deng, H.; Chai, Y.; Yuan, R.; Yuan, Y. *Anal. Chem.* **2020**, *92*, 8364−8370.
(28) Zhou, Y.; Shi, Y.; Wang, F.-B.; Xia, X.-H. *Anal. Chem.* **2019**, *91*, 2759−2767.
(29) Lin, Y.; Zhou, Q.; Tang, D. *Anal. Chem.* **2017**, *89*, 11803−11810.
(30) Zhang, K.; Lv, S.; Tang, D. *Anal. Chem.* **2019**, *91*, 10049−10055.
(31) Zeng, R.; Luo, Z.; Su, L.; Zhang, L.; Tang, D.; Niessner, R.; Knopp, D. *Anal. Chem.* **2019**, *91*, 2447−2454.
(32) Yu, S.-Y.; Mei, L.-P.; Xu, Y.-T.; Xue, T.-Y.; Fan, G.-C.; Han, D.-M.; Chen, G.; Zhao, W.-W. *Anal. Chem.* **2019**, *91*, 3800−3804.
(33) Chen, F.-Z.; Han, D.-M.; Chen, H.-Y. *Anal. Chem.* **2020**, *92*, 8450−8458.
(34) Fu, Y.; Zou, K.; Liu, M.; Zhang, X.; Du, C.; Chen, J. *Anal. Chem.* **2020**, *92*, 1189−1196.
(35) Chu, Y.; Deng, A.-P.; Wang, W.; Zhu, J.-J. *Anal. Chem.* **2019**, *91*, 3619−3627.
(36) Li, C.; Lu, W.; Zhou, X.; Pang, M.; Luo, X. *Anal. Chem.* **2018**, *90*, 14239−14246.
(37) Simmel, F. C.; Yurke, B.; Singh, H. R. *Chem. Rev.* **2019**, *119*, 6326−6369.
(38) Zhang, D. Y.; Turberfield, A. J.; Yurke, B.; Winfree, E. *Science* **2007**, *318*, 1121−1125.
(39) Lv, Y.; Cui, L.; Peng, R.; Zhao, Z.; Qiu, L.; Chen, H.; Jin, C.; Zhang, X. B.; Tan, W. *Anal. Chem.* **2015**, *87*, 11714−11720.
(40) Zhang, N.; Shi, X.-M.; Guo, H.-Q.; Zhao, X.-Z.; Zhao, W.-W.; Xu, J.-J.; Chen, H.-Y. *Anal. Chem.* **2018**, *90*, 11892−11898.
(41) Li, H.; Li, Y.; Li, J.; Yang, F.; Xu, L.; Wang, W.; Yao, X.; Yin, Y. *Anal. Chem.* **2020**, *92*, 4094−4100.
(42) Wang, Q.; Wang, X.; Wu, Y. *Photochem. Photobiol.* **2019**, *95*, 895−900.
(43) Zadeh, J. N.; Steenberg, C. D.; Bois, J. S.; Wolfe, B. R.; Pierce, M. B.; Khan, A. R.; Dirks, R. M.; Pierce, N. A. *J. Comput. Chem.* **2011**, *32*, 170−173.
(44) Guo, Q.; Yu, Y.; Zhang, H.; Cai, C.; Shen, Q. *Anal. Chem.* **2020**, *92*, 5302−5310.
(45) Masud, M. K.; Na, J.; Lin, T.-E.; Malgras, V.; Preet, A.; Ibn Sina, A. A.; Wood, K.; Billah, M.; Kim, J.; You, J.; Kani, K.; Whitten, A. E.; Salomon, C.; Nguyen, N.-T.; Shiddiky, M. J. A.; Trau, M.; Hossain, M. S. A.; Yamauchi, Y. *Biosen. Bioelectron.* **2020**, *168*, 112429.
(46) Park, H.; Masud, M. K.; Na, J.; Lim, H.; Phan, H.-P.; Kaneti, Y. V.; Alothman, A. A.; Salomon, C.; Nguyen, N.-T.; Hossain, M. S. A.; Yamauchi, Y. *J. Mater. Chem. B* **2020**, DOI: 10.1039/D0TB02003F.
(47) Wang, F.; Chu, Y.; Ai, Y.; Chen, L.; Gao, F. *Microchim. Acta* **2019**, *186*, 116−124.
(48) Liu, Y.; Shen, T.; Li, J.; Gong, H.; Chen, C.; Chen, X.; Cai, C. *ACS Sens.* **2017**, *2*, 1430−1434.
(49) Tang, Y.; Liu, M.; Zhao, Z.; Li, Q.; Liang, X.; Tian, J.; Zhao, S. *Microchim. Acta* **2019**, *186*, 133.
(50) Qi, T.; Song, C.; He, J.; Shen, W.; Kong, D.; Shi, H.; Tan, L.; Pan, R.; Tang, S.; Lee, H. K. *Anal. Chem.* **2020**, *92*, 5033−5040.
(51) Hao, N.; Lu, J.; Chi, M.; Xiong, M.; Zhang, Y.; Hua, R.; Wang, K. *J. Mater. Chem. B* **2019**, *7*, 1133−1141.
(52) Li, B.; Yin, H.; Zhou, Y.; Wang, M.; Wang, J.; Ai, S. *Sens. Actuators, B* **2018**, *255*, 1744−1752.
(53) Wang, M.; Yin, H.; Zhou, Y.; Sui, C.; Wang, Y.; Meng, X.; Waterhouse, G. I. N.; Ai, S. *Biosen. Bioelectron.* **2019**, *128*, 137−143.

https://dx.doi.org/10.1021/acs.analchem.0c03580
Anal. Chem. XXXX, XXX, XXX−XXX